Distinguishing primordial magnetic fields from inflationary tensor perturbations in the cosmic microwave background

Yilun Guan*

Department of Physics and Astronomy, University of Pittsburgh, Pittsburgh, Pennsylvania 15260, USA and Dunlap Institute for Astronomy and Astrophysics, University of Toronto, 50 Saint George Street, Toronto, Ontario M5S 3H4, Canada

Arthur Kosowsky

Department of Physics and Astronomy, University of Pittsburgh, Pittsburgh, Pennsylvania 15260, USA

(Received 10 May 2022; accepted 2 August 2022; published 7 September 2022)

A claimed detection of cosmological tensor perturbations from inflation via B-mode polarization of the cosmic microwave background requires distinguishing other possible B-mode sources. One such potential source of confusion is primordial magnetic fields. For sufficiently low-amplitude B-mode signals, the microwave background temperature and polarization power spectra from power-law tensor perturbations and from a power-law primordial magnetic field are indistinguishable. However, we show that such a magnetic field will induce a small-scale Faraday rotation which is detectable using four-point statistics analogous to gravitational lensing of the microwave background. The Faraday rotation signal will distinguish a magnetic-field-induced B-mode polarization signal from tensor perturbations for effective tensor-to-scalar ratios larger than 0.001, detectable in upcoming polarization experiments.

DOI: 10.1103/PhysRevD.106.063505

I. INTRODUCTION

One of the primary goals of the next-generation of cosmic microwave background (CMB) experiments is to detect the primordial B-mode polarization signal from the tensor perturbations generated by inflation. A detection of this signal would be compelling evidence of inflation and help determine the physical mechanism of inflation. While early Universe inflation generically predicts the production of metric tensor perturbations with a nearly scale-invariant spectrum via quantum fluctuations in the gravitational field, the amplitude of the tensor spectrum can vary greatly between plausible inflation models.

The current best constraint on the tensor-to-scalar ratio is $r < 0.056$ at the 95% confidence level through a combined analysis of *Planck* and BICEP2 [1]. The next generation of large-angle CMB polarization experiments—including the Simons Observatory [2], BICEP3 [3], LiteBIRD [4], and CMB-S4 [5]—will have the sensitivity and frequency range to reduce this bound to $r = 10^{-3}$ or below. However, the tensor perturbations from inflation are not the only source of B-mode polarization in the CMB. Foregrounds and lensing, in particular, are both known to contribute to B-mode polarization. Even regions of the sky with expected low Galactic foregrounds still have polarized foregrounds which are substantially larger than current upper limits on any primordial B-mode polarization component [6–8]. In order to separate foregrounds from cosmological polarization signals, the coming generation of large-angle B-mode experiments (BICEP3, Simons Observatory, LiteBIRD) will measure in many frequency bands, and test the spatial isotropy and Gaussianity of any signal.

It has also been known for a long time that the lensing B-mode signal has a low-ℓ contribution whose power spectrum can be mistaken for or confused with a low-amplitude primordial signal [9]. B-mode polarization from lensing has been detected in cross correlation by SPT [10] and ACT [11]. Great progress has been made in measuring lensing signals through their non-Gaussian four-point signature (see, e.g., Ref. [12]), and maps of the lensing deflection potential have been reconstructed with data from ACT [13], SPT [14], and *Planck* [15]. In principle, this can be done with very high precision, given clean enough maps with low enough noise (see, e.g., Refs. [16,17]), but in practice there is a limit to how well low-ℓ lensing can be reconstructed due to having imperfect data with nonzero noise. For example, although detecting a signal with $r \sim 10^{-6}$ is theoretically achievable in the absence of any systematic errors, sky cuts, and foregrounds [17], realistic forecasts that include such effects generally predict a much lower sensitivity at the level of $\sigma(r) \sim 10^{-3}$ [18].

Foregrounds and lensing are the two most important confusion signals for primordial B-mode polarization, and detailed modeling of those are well in hand (see Ref. [19]

*yilun.guan@utoronto.ca

for a review). What else could confuse us? Perhaps the next most likely signal would be from a primordial magnetic field. Such concern has previously been brought up in, e.g., Refs. [20,21] and discussed in Ref. [22]. The extent to which we can distinguish the two signals, given imperfect data with nonzero noise, motivates this paper.

Magnetic fields are ubiquitous in the Universe today, with typical strengths of a few microgauss in galaxies and galaxy clusters (see, e.g., Refs. [23–25] for reviews). Furthermore, evidence from the nonobservation of inverse Compton cascade γ rays from TeV blazars [26] suggests that magnetic fields are present in the intergalactic medium, with a lower limit of around 10^{-7} nG on Mpc scales. However, the physical origin of the cosmic magnetic field remains poorly understood. One intriguing possibility is that cosmic magnetic fields are present before structure formation and are produced in the very early Universe, such as during inflation [27] or during a phase transition [28]. Magnetic fields that are present before the decoupling of CMB photons are generally known as primordial magnetic fields.

If present, a primordial magnetic field impacts both the ionization history of the Universe and structure formation, leaving imprints on the CMB and the matter power spectrum [29]. In particular, primordial magnetic fields source scalar, vector, and tensor metric perturbations, and influence baryon physics through the Lorentz force. In addition, primordial magnetic fields also introduce a net rotation of the linear polarization of the CMB photons through an effect known as Faraday rotation, which leaves an observable frequency-dependent signal in the CMB polarization pattern [30,31].

The amplitude of the comoving magnetic field B_0 present today is constrained to be no more than a few nG (see, e.g., Refs. [32,33]). However, it has been previously shown that a magnetic field with a mean amplitude of around 1 nG and a power-law power spectrum can generate a CMB B-mode power spectrum similar to that of an inflationary tensor-mode signal with tensor-to-scalar ratio $r \simeq 0.004$ [22]. This is roughly the limiting tensor amplitude that will be detected by upcoming CMB experiments. Hence, a lack of knowledge of the primordial magnetic field may potentially lead us to a wrong conclusion if a B-mode polarization signal were to be detected by upcoming CMB experiments.

In this work we aim to review and reevaluate, with particular focus on the upcoming CMB experiments, the potential degeneracy between a B-mode signal from a primordial magnetic field model and that from primordial gravitational waves. In particular, we evaluate the degeneracy for different tensor-to-scalar ratios r, in the context of experimental configurations that model the capabilities of upcoming CMB experiments. We also investigate the extent to which we can break the degeneracy with Faraday rotation from the magnetic field, at both the power-spectrum level and the map level. In particular, as we show in Sec. V, quadratic estimation of Faraday rotation at 90 GHz gives a much more significant detection of magnetic fields than the power spectrum for a given map noise and resolution; for a tensor-mode signal at the level of $r = 10^{-3}$, Faraday rotation clearly breaks the power spectrum degeneracy between tensor perturbations and magnetic fields.

This paper is organized as follows. In Sec. II, we review the basics of the primordial magnetic field. In Sec. III, we summarize the primordial magnetic field contributions to the CMB power spectrum and evaluate the potential confusion with the tensor-mode signal from inflation. In Sec. IV, we briefly review the physics of Faraday rotation from primordial magnetic fields and discuss to what extent this effect allows us to break the degeneracy between primordial magnetic fields and primordial tensor-mode signals. In Sec. V, we summarize the reconstruction of Faraday rotation through quadratic estimators and then discuss to what extent it helps us break the degeneracy. Finally, we discuss our results and conclude in Sec. VI.

II. PRIMORDIAL MAGNETIC FIELDS

A. Statistics of stochastic matgnetic fields

We consider a stochastic background of magnetic fields generated prior to recombination and assume that the magnetic field is weak enough to be treated as a perturbation to the mean energy density of the Universe. As the Universe is highly conductive prior to recombination, any electric field quickly dissipates. On scales larger than the horizon, the magnetic field is effectively "frozen in" due to the negligible magnetic diffusion on cosmological scales. Hence, the conservation of magnetic flux gives the scaling relation $B^i(x^j,\tau) = B^i(x^j)/a(\tau)^2$, where a is the scale factor, τ is the conformal time, and x^j are the comoving coordinates. We also assume that the stochastic background of magnetic fields follows the statistics of a Gaussian random field, and the energy density of magnetic fields, which scales quadratically with the magnetic field strength ($\propto B^2$), follows chi-squared statistics. In Fourier space,[1] the statistics of the magnetic field can be completely described by its two-point correlations

$$\langle B_i^*(\mathbf{k}) B_j(\mathbf{k}')\rangle = (2\pi)^3\delta^{(3)}(\mathbf{k}-\mathbf{k}') \times [P_{ij}P_B(k) + i\epsilon_{ijl}\hat{k}_l P_H(k)], \quad (1)$$

where $P_{ij} \equiv \delta_{ij} - \hat{k}_i\hat{k}_j$ is a projection operator onto the transverse plane to $\hat{k}$ such that $P_{ij}k^j = 0$, and ϵ_{ijl} is the total antisymmetric tensor. Here P_H and P_B refer to the helical and nonhelical parts of the magnetic field power spectrum,

[1]In this paper we use the following Fourier convention: $\tilde{f}(\mathbf{k}) = \int d^3x e^{i\mathbf{k}\cdot\mathbf{x}} f(\mathbf{x})$, and $f(\mathbf{x}) = \frac{1}{(2\pi)^3}\int d^3k e^{-i\mathbf{k}\cdot\mathbf{x}}\tilde{f}(\mathbf{k})$.

respectively. For the sake of simplicity, we assume that the helical magnetic field component vanishes, though we should note that a helical magnetic field is predicted by some proposed magnetogenesis scenarios (see, e.g., Refs. [34,35]).

We assume that the power spectrum of the magnetic field follows a power law with a cutoff scale k_D, given by

$$P_B = A_B k^{n_B}, \qquad k \leq k_D, \tag{2}$$

which vanishes for $k > k_D$. The dissipation scale k_D reflects the suppression of the magnetic field due to radiation viscosity on small scales. A_B and n_B denote the amplitude and spectral index of the magnetic field power spectrum, respectively, both of which depend on the specific magnetogenesis scenario. In particular, an inflationary magnetogenesis model prefers a scale-invariant spectrum with a spectral index $n_B \approx 3$, while a causally generated magnetic field in the post-inflationary epoch prefers a spectrum with $n_B \geq 2$ [21].

The assumption that the magnetic field is "frozen in" and follows a power law with a cutoff scale k_D is only an approximation. Magnetohydrodynamic simulations (e.g., Refs. [36–38]) have shown that magnetic fields tend to source turbulence on scales smaller than the horizon. However, such an effect is expected to have a negligible impact on the results in this paper as it mostly affects the small-scale magnetic fields, whereas (as we discuss in Sec. III) only the large-scale magnetic modes are degenerate with a primordial tensor mode signal. Thus, we neglect subhorizon plasma dynamics.

In addition, following a common convention in the literature, we smooth the magnetic field with a Gaussian kernel $f_\lambda(x) = N \exp(-x^2/2\lambda^2)$ on a comoving scale λ. The magnetic field fluctuation on the comoving scale λ can then be characterized by

$$B_\lambda^2 \equiv \langle \mathbf{B}_\lambda(\mathbf{x}) \cdot \mathbf{B}_\lambda(\mathbf{x}) \rangle = \frac{1}{\pi^2} \int_0^\infty dk k^2 e^{-k^2\lambda^2} P_B(k), \tag{3}$$

which is related to the power spectrum amplitude A_B by

$$A_B = \frac{(2\pi)^{n_B+5} B_\lambda^2}{2\Gamma(\frac{n_B+3}{2}) k_\lambda^{n_B+3}}. \tag{4}$$

The damping scale k_D can also be approximated as [39]

$$k_D = (5.5 \times 10^4)^{\frac{1}{n_B+5}} \left(\frac{B_\lambda}{1\ \mathrm{nG}}\right)^{-\frac{2}{n_B+5}} \left(\frac{2\pi}{\lambda/\mathrm{Mpc}}\right)^{\frac{n_B+3}{n_B+5}} \times h^{\frac{1}{n_B+5}} \left(\frac{\Omega_b h^2}{0.022}\right)^{\frac{1}{n_B+5}} \Bigg|_{\lambda=1\ \mathrm{Mpc}} \mathrm{Mpc}^{-1}, \tag{5}$$

where h is the reduced Hubble parameter defined as $h \equiv H_0/100\ \mathrm{km\,s^{-1}\,Mpc^{-1}}$.

B. Magnetic perturbations

Consider a particular realization of a stochastic magnetic field, with the magnitude of the field at x and conformal time τ given by $B^i(\mathbf{x}, \tau)$. Its energy-momentum tensor can be written as

$$\begin{aligned} T^0{}_0 &= -\frac{1}{8\pi a^4} B^2(\mathbf{x}), \\ T^0{}_i &= T^i{}_0 = 0, \\ T^i{}_j &= \frac{1}{4\pi a^4}\left[\frac{1}{2} B^2(\mathbf{x})\delta^i{}_j - B^i(\mathbf{x}) B_j(\mathbf{x})\right], \end{aligned} \tag{6}$$

where we have used the "freeze-in" condition $B^i(\mathbf{x}, \tau) = B^i(\mathbf{x})/a(\tau)^2$. Since $\rho_B \equiv T^0{}_0 \propto a^{-4}$ scales the same way as the photon energy density, one can reparametrize the magnetic field perturbation relative to the photon density ρ_γ and pressure p_γ as [29]

$$\begin{aligned} T^0{}_0 &= -\rho_\gamma \Delta_B, \\ T^i{}_j &= p_\gamma(\Delta_B \delta^i_j + \Pi^i{}_{Bj}), \end{aligned} \tag{7}$$

where Δ_B denotes the scalar perturbations sourced by magnetic fields relative to the radiation energy density, and $\Pi^i{}_{Bj}$ denotes the anisotropic stress from magnetic fields which can be further decomposed into scalar-, vector-, and tensor-type perturbations.

Initial conditions of magnetically induced perturbation modes can be decomposed into three types: (1) compensated [40,41], (2) passive [29,42], and (3) inflationary [43]. In particular, compensated magnetic modes arise when the magnetic contributions to the metric perturbations are compensated by fluid modes to the leading order on superhorizon scales. They include the contributions from magnetic fields after neutrino decoupling, and are finite in the $\tau \to 0$ limit. The passive magnetic modes, on the other hand, account for the magnetic contribution prior to neutrino decoupling. In this period, the Universe is dominated by a tightly coupled radiative fluid which prevents any anisotropic stress from developing. Without neutrino free-streaming, the magnetic field acts as the only source of anisotropic stress, leading to a logarithmically growing mode [42]. This mode survives neutrino decoupling as a constant offset on the amplitude of the nonmagnetic mode. Inflationary magnetic modes, as another type of initial condition, depend on the specific generation mechanism [43], and are therefore not considered in this paper in order to maintain the generality of our results to different magnetic field models.

We also note that several other isocurvature modes involving magnetic fields exist, as outlined in Refs. [44,45]. In this work we focus only on the "adiabatic" mode because its CMB anisotropy power spectrum is more difficult to distinguish from the measured power spectrum

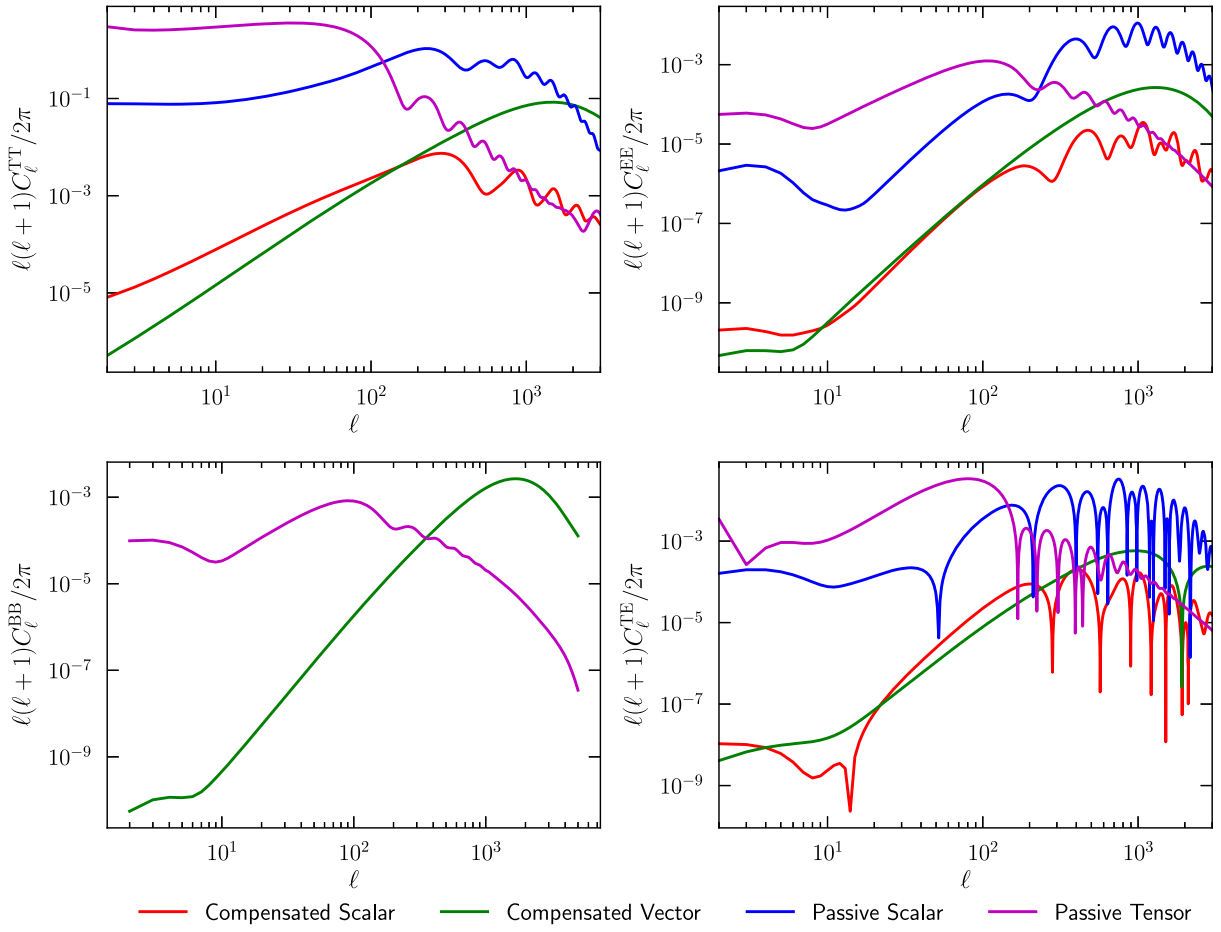

FIG. 1. Contributions of different magnetic modes to the CMB power spectra (in units of $\mu\mathrm{K}^2$) from a stochastic background of primordial magnetic fields with $\mathrm{B}_{1\ \mathrm{Mpc}} = 1$ nG, $\log_{10}\tau_B/\tau_\nu = 17$, and $n_B = -2.9$ (nearly scale invariant) generated using MagCAMB.

(which is consistent with adiabatic perturbations with a power-law initial power spectrum in standard ΛCDM). Isocurvature modes will generate power spectra with acoustic peaks out of phase with the measured power spectrum [44] which, for a given amplitude of magnetic field, will make isocurvature modes *easier* to detect in the CMB power spectra than adiabatic modes of the same amplitude. Thus, we expect the conclusion of our study to also hold for isocurvature modes, if not stronger, and we leave a more thorough analysis to future work.

From this physical picture it is apparent that the size of the perturbations from magnetic fields depends on the epoch of their generation relative to the epoch of neutrino decoupling, as can be parametrized by $\log_{10}(\tau_\nu/\tau_B)$, where τ_ν is the neutrino decoupling time and τ_B is the magnetic field generation time. Though the exact number for this quantity remains unknown and can be model dependent, we assume $\log_{10}(\tau_\nu/\tau_B) = 17$ for simplicity, following Ref. [33]. In addition, the magnetic field also introduces a Lorentz force acting on the baryons in the primordial plasma. It effectively augments the pressure perturbations of the baryon-photon fluid which prevent photons and baryons from falling into their gravitational wells. This effect is analogous to a change in the baryon energy density which affects the sound speed of the baryon-photon fluid and changes its acoustic oscillations [46–48].

III. IMPACTS ON CMB POWER SPECTRA

A primordial magnetic field influences CMB anisotropies through both its metric perturbations and the Lorentz force, and generates perturbations of scalar, vector, and tensor types. We make use of the publicly available code MagCAMB[2] [32] which extends the Boltzmann code CAMB [49] to include the effects of a primordial magnetic field discussed in Sec. II. In Fig. 1 we show an example set of CMB power spectra that are sourced by a stochastic primordial magnetic field with $B_{1\ \mathrm{Mpc}} = 1$ nG and a nearly scale-invariant spectrum ($n_B = -2.9$). Contributions from different magnetic modes are plotted in different colors, from which one observes that the passive tensor-mode signal in $C_\ell^{\rm BB}$ has significant power at $\ell \lesssim 100$ resembling

[2]https://github.com/alexzucca90/MagCAMB.

that of an inflationary tensor-mode signal and hence may pose a possible source of confusion. On the other hand, the compensated vector-mode contribution dominates at $\ell \gtrsim 1000$ in both C_ℓ^{TT} and C_ℓ^{BB} which is not degenerate with the inflationary tensor-mode signal. Hence, this vector-mode perturbation from primordial magnetic fields gives us a potential way to break the degeneracy.

To evaluate the extent of the confusion for upcoming CMB experiments, we simulate different sets of CMB power spectra using CAMB with the standard ΛCDM model and the *Planck* best-fit cosmological parameters as our fiducial model [50], while varying the tensor-to-scalar ratio r to reflect different science targets, with the spectral index n_T fixed by the slow-roll inflation consistency relation $n_T = -r/8$. We consider several toy-model full-sky microwave background experiments specified by angular resolution and map sensitivity. In addition, we simulate the observed power spectra for each experiment with an idealized noise model given by

$$N_\ell = w^{-1} \exp\left(\ell(\ell+1)\theta^2/8\ln 2\right), \tag{8}$$

where $w^{-1/2} \equiv \sqrt{4\pi\sigma_{\mathrm{pix}}^2/N_{\mathrm{pix}}}$ denotes the expected noise level of an experiment, with σ_{pix} being the per-pixel noise level, N_{pix} the total number of pixels, and θ the FWHM size of a Gaussian telescope beam. We also assume that the polarization and temperature noise are related simply by $(\sigma_{\mathrm{pix}}^{\mathrm{P}})^2 = 2(\sigma_{\mathrm{pix}}^{\mathrm{T}})^2$.

In Table I we list the toy-model experiments (Expts) considered in this work. In particular, Expts A and B approximate the capabilities of the Simons Observatory Large Aperture Telescope (SO LAT) and Small Aperture Telescope (SO SAT), respectively. Expt C1 represents a combined constraint with both of these experiments. Expt C2 represents the capability of the anticipated CMB-S4 experiment, while Expt C3 is the limit of a noiseless CMB map so that the power spectrum uncertainty is due entirely to cosmic variance.

TABLE I. Different sets of experimental parameters considered in this paper. Expt A represents a ground-based small-aperture telescope, while Expt B represents a ground-based large-aperture telescope. Expts C1, C2, and C3 represent a combination of Expts A and B at various noise levels.

Name	Beam (arcmin)	Noise (μK arcmin)	ℓ_{min}	ℓ_{max}	f_{sky}
A	17	2	30	1000	0.1
B	1.4	6	30	3000	0.4
C1	17	2	30	1000	0.1
	1.4	6	30	3000	0.4
C2	17	1	30	1000	0.1
	1.4	2	30	3000	0.4
C3	17	0	30	1000	0.1
	1.4	0	30	3000	0.4

We compute Markov chain Monte Carlo (MCMC) model fitting to find the best-fit cosmologies for two competing models: (1) a model with a nonzero tensor-to-scalar ratio r but no primordial magnetic field contribution (ΛCDM + r hereafter), and (2) a model with $r = 0$ but nonzero primordial magnetic field contribution (ΛCDM + PMF hereafter). The Markov chain varies the standard cosmological parameters, plus either the tensor-to-scalar ratio or the primordial magnetic field amplitude and power spectrum index (see Appendix A for more details on the MCMC model fitting and example results from the Markov chains). The log-likelihood for a given model is taken as [51]

$$-2\ln\mathcal{L}(\{\hat{\mathbf{C}}_\ell\}|\{\mathbf{C}_\ell\}) = \sum_l (2l+1)\{\mathrm{Tr}[\hat{\mathbf{C}}_\ell \mathbf{C}_\ell^{-1}] - \ln|\hat{\mathbf{C}}_\ell \mathbf{C}_\ell^{-1}| - 3\}, \tag{9}$$

where $\mathbf{C}_\ell$ contains the theory power spectra given by

$$\mathbf{C}_\ell \equiv \begin{pmatrix} C_\ell^{\mathrm{TT}} & C_\ell^{\mathrm{TE}} & 0 \\ C_\ell^{\mathrm{TE}} & C_\ell^{\mathrm{EE}} & 0 \\ 0 & 0 & C_\ell^{\mathrm{BB}} \end{pmatrix}, \tag{10}$$

and $\hat{\mathbf{C}}_\ell$ contains the observed power spectra given by

$$\hat{\mathbf{C}}_\ell \equiv \frac{1}{2\ell+1}\sum_m \boldsymbol{a}_{\ell m}\boldsymbol{a}_{\ell m}^\dagger, \tag{11}$$

with $\boldsymbol{a}_{\ell m} \equiv (a_{\ell m}^{\mathrm{T}} a_{\ell m}^{\mathrm{E}} a_{\ell m}^{\mathrm{B}})^T$. Note that the full set of power spectra—C_ℓ^{TT}, C_ℓ^{EE}, C_ℓ^{BB}, and C_ℓ^{TE}—are used in the model fitting.

Specifically, the simulated power spectrum is generated with the ΛCDM + r model, which we then fit with a ΛCDM + PMF model to find degenerate magnetic field models in terms of CMB power spectra. Although in theory the expected power spectra from the two competing models are not completely degenerate due to, for instance, the vector-mode signal from the primordial magnetic field, in practice the difference may not be detectable at a given experimental noise level, especially when $B_{1\ \mathrm{Mpc}} \lesssim 1$ nG. By computing the $\Delta\chi^2$ between the two best-fit models, we evaluate the extent of the degeneracy between the ΛCDM + r model and the ΛCDM + PMF model at various r targets and experiment sensitivities, as listed in Table I.

A. Fiducial cosmology with $r = 0.01$

We first consider a target of $r = 0.01$ which is one of the primary goals of the upcoming CMB experiments such as the Simons Observatory [2]. In particular, the Simons Observatory will have two separate instruments for

measuring different angular scales of the CMB power spectrum: a large-aperture telescope which mainly focuses on small-angle CMB anisotropies, and a small-aperture telescope which mainly focuses on the large-angle CMB anisotropies. As the tensor-mode signal from inflation is expected to show up predominantly in the large angular scales, it is the main target of the SO SAT experiment.

Suppose that we live in a universe that is well described by a $\Lambda\mathrm{CDM}+r$ model with $r=0.01$, and we measure the CMB power spectrum with an SO SAT–like experiment, specified as Expt A in Table I. We simulate the observed CMB power spectra for Expt A between angular scales of $\ell_{\mathrm{min}}=30$ and $\ell_{\mathrm{max}}=3000$, with a sky fraction of $f_{\mathrm{sky}}=0.3$, to account for the effect of partial sky coverage from a ground-based experiment.

We then fit the simulated data with both the $\Lambda\mathrm{CDM}+r$ and $\Lambda\mathrm{CDM}+\mathrm{PMF}$ models. The resulting B-mode polarization power spectra C_ℓ^{BB} for the two best-fit models are shown in Fig. 2, compared to the simulated data. It shows that the two competing models can be highly degenerate over the angular scales probed by the simulated experiment (Expt A; $30\lesssim\ell\lesssim3000$), with a difference much smaller than the variance of the observed data. To be more specific, one can model the variance of the observed data as [52]

$$\sigma^2(C_\ell)=\frac{2}{(2\ell+1)f_{\mathrm{sky}}}(C_\ell+N_\ell)^2 \tag{12}$$

and compare it to the difference between the two sets of best-fit power spectra, as shown in Fig. 3. The difference in the best-fit power spectra is around 2 orders of magnitude below the expected variance of the observed power spectrum, indicating that breaking the degeneracy between the two models is impossible without additional information. The corresponding difference in χ^2 between these two best-fit models is $\Delta\chi^2\simeq0.1$

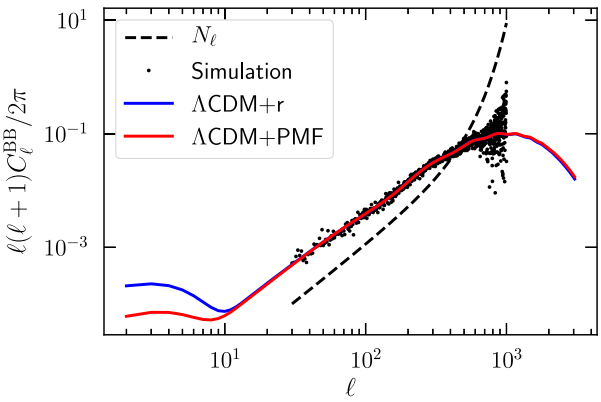

FIG. 2. Best-fit C_ℓ^{BB} power spectra (in units of $\mu\mathrm{K}^2$) for the $\Lambda\mathrm{CDM}+r$ (blue) and $\Lambda\mathrm{CDM}+\mathrm{PMF}$ (red) models, to an underlying tensor cosmology with $r=0.01$ and map noise Expt A in Table I. The black dots represent the simulated data after removing noise model UNCLEAR, and the black dashed line represents the noise model.

The degeneracy between the two models is nottoo surprising because on large angular scales ($\ell\lesssim100$) the passive tensor mode dominates over the other contributions from the primordial magnetic field, and the passive tensor mode is mathematically equivalent to the inflationary tensor-mode signal; the degeneracy is unavoidable if one observes only on large angular scales. On the other hand, one does see a noticeable difference between the two models at $\ell\lesssim10$, indicating that the two models are not completely degenerate on all angular scales. This is expected because on small angular scales ($\ell\gtrsim1000$) the compensated vector mode signal from a primordial magnetic field starts to dominate over the other magnetic modes in the C_ℓ^{BB} power spectrum. This difference on small scales gets minimized by the best-fit model, leading to the difference seen at $\ell\lesssim10$. This also implies that the small-scale CMB anisotropies contain crucial information that helps break the degeneracy between $r=0.01$ in tensor perturbations and a primordial magnetic field.

In Fig. 4 we show the posterior distributions of the magnetic field parameters ($\mathrm{B}_{1\ \mathrm{Mpc}}$ and n_B) from the $\Lambda\mathrm{CDM}+\mathrm{PMF}$ model fitting an inflationary tensor perturbation at $r=0.01$. Specifically, we obtain a best-fit primordial magnetic field model with $\mathrm{B}_{1\ \mathrm{Mpc}}=1.42^{+0.42}_{-0.54}$ nG at the 68% confidence level, on par with the observational constraints set by *Planck* in 2015 [33]. We also note that a nearly scale-invariant spectrum, with a spectral index of $n_B<-2.49$, is preferred by the simulated data, which we find to be a generic feature of the $\Lambda\mathrm{CDM}+\mathrm{PMF}$ models degenerate to $\Lambda\mathrm{CDM}+r$. An apparent degeneracy between the amplitude of the magnetic field $\mathrm{B}_{1\ \mathrm{Mpc}}$ and the magnetic spectral index n_B can also be seen. This is because as n_B increases, the power spectrum of primordial magnetic fields tilts toward smaller scales, leading to less power in the large-scale modes which Expt A (or an SO SAT–like experiment) is sensitive to, and thus the loss of power gets compensated by a stronger magnetic field.

Now suppose that one obtains additional observations from a large-aperture telescope like the SO LAT, specified as Expt B in Table I, which strongly constrains the small-scale CMB anisotropies. One can then combine its constraining power with Expt A to jointly constrain the primordial magnetic field on both small and large angular scales. For simplicity, we simulate the observed power spectra of the combined constraint by simulating two separate experiments with the same underlying CMB realization and combining them trivially by using the

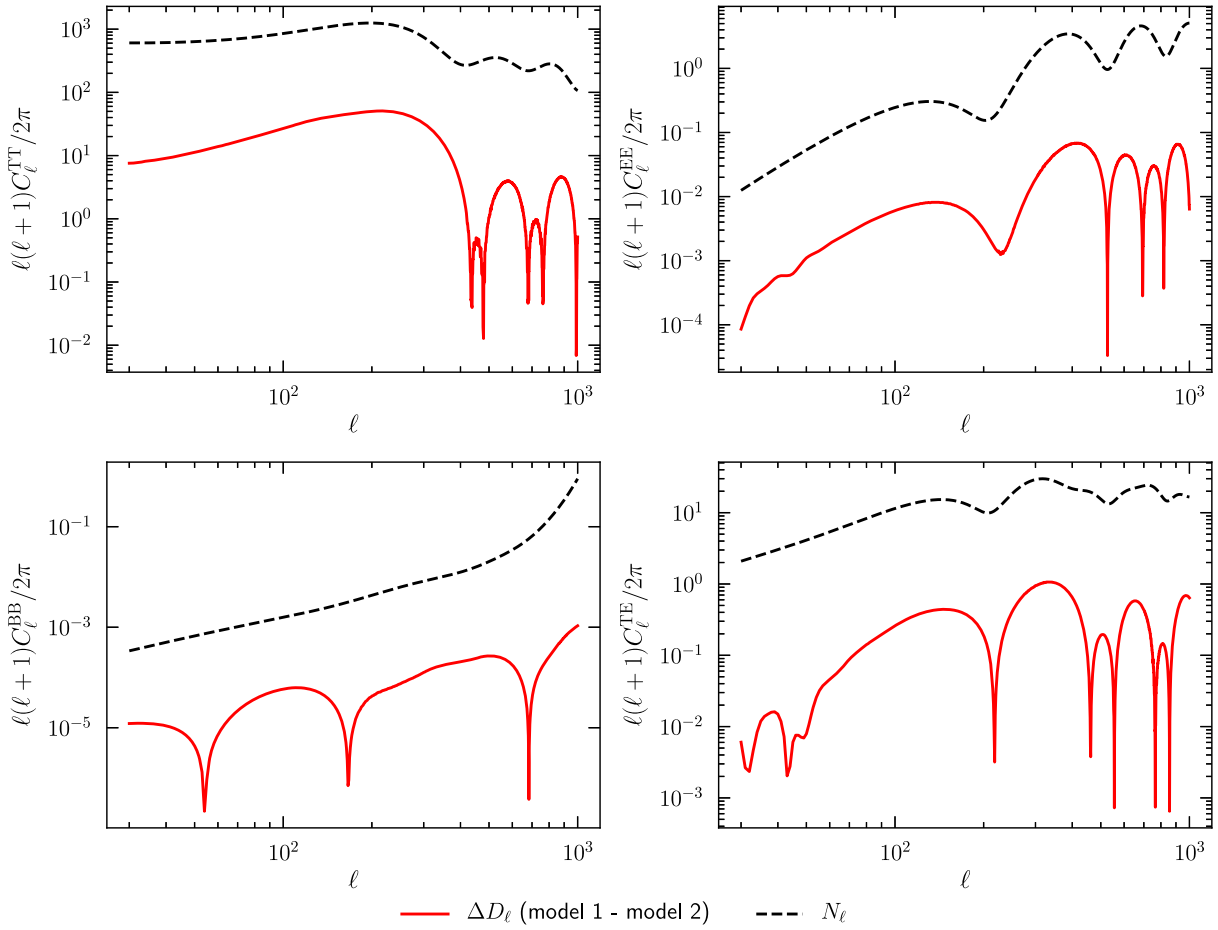

FIG. 3. Difference of the two best-fit CMB power spectra in Fig. 2 (red solid line) and the analytic covariance of the simulated power spectrum (black dashed line).

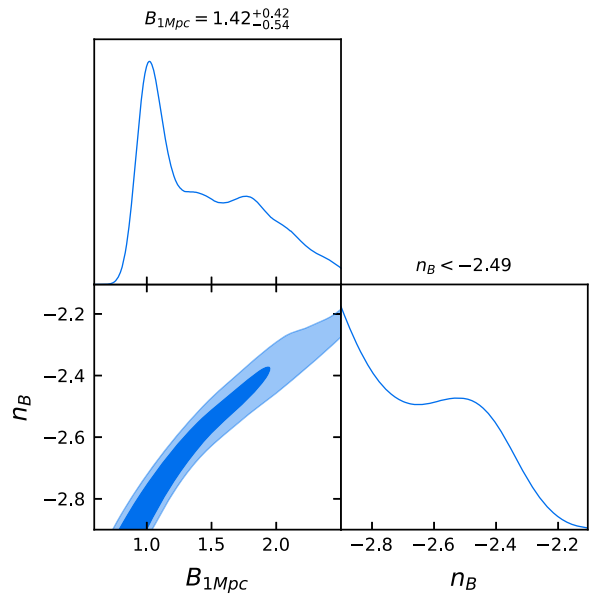

FIG. 4. Joint posterior distributions for the ΛCDM + PMF model parameters after fitting the simulated data (generated with a ΛCDM + r model with $r = 0.01$) to a ΛCDM + PMF model.

experiment that gives the lowest variance at each ℓ to avoid mode double counting.

In Fig. 5, we show how the joint posterior distribution of the magnetic field parameters ($B_{1\ \mathrm{Mpc}}$ and n_B) changes after we add the data from Expt B to the constraint. The degeneracy between n_B and $B_{1\ \mathrm{Mpc}}$ is broken when the additional observations from Expt B (or an SO LAT–like experiment) are included which tightly constrains the small-scale modes of the primordial magnetic field. The joint constraint leads to a much tighter allowed parameter space (shown as the red contour) favoring a primordial magnetic field with $B_{1\ \mathrm{Mpc}} \sim 1$ nG and a scale-invariant spectrum. We find a $\Delta\chi^2 \simeq -2.5$ between the best-fit ΛCDM + r model and the ΛCDM + PMF model, showing a stronger preference for the ΛCDM + r model. This improvement in $\Delta\chi^2$ is driven by improved sensitivity in the small angular scales which severely constrain the compensated vector mode from primordial magnetic field, dominating at $\ell \gtrsim 1000$ and with no degenerate signal in ΛCDM + r. This indicates that if an apparent primordial B-mode signal is detected at an amplitude of around $r = 0.01$, a joint constraint using both large and small

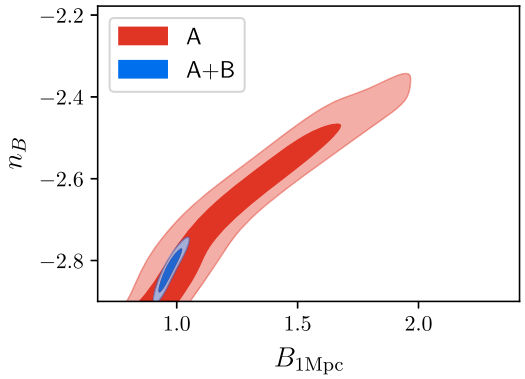

FIG. 5. Joint posterior distributions of the magnetic field parameters after fitting a ΛCDM + PMF model to the simulated CMB power spectra with a fiducial model of inflationary tensor modes with $r = 0.01$. The red contour shows the posterior distribution obtained from Expt A only, while the blue contour shows the posterior distribution obtained from a joint constraint from both Expt A and Expt B, as specified in Table I. Contour levels indicate the 68% and 95% confidence levels, respectively.

angular scale measurements is a promising approach to rule out a degenerate ΛCDM + PMF model.

B. Lower-r targets

In addition to the fiducial model with $r = 0.01$ discussed in the preceding section, we also repeat the study in Sec. III A for different targets of r ranging from 0.001 to 0.010, and compute $\Delta\chi^2$ between the two best-fit models for each set of the simulations of a given r. In particular, we consider three sets of combined observations specified as Expts C1, C2, C3 in Table I. Expt C1 represents the set of observations considered in Sec. III A as a joint constraint of Expts A and B, Expt C2 represents a similar set of experiments with lower noise levels, and Expt C3 represents the same set of experiments in a noiseless limit.

The results of model fitting show that the degenerate ΛCDM + PMF models generally favor a nearly scale-invariant spectrum ($n_B \simeq -2.9$) with $\mathrm{B}_{1\ \mathrm{Mpc}} \lesssim 0.8$ nG, which is below the current observational limits. Figure 6 shows how the amplitude of the magnetic field in the degenerate ΛCDM + PMF model varies with r. This is useful because it provides a look-up table of degenerate parameter spaces between the two models, allowing one to easily identify the degenerate magnetic field model to a given r target. It shows that, in general, one only needs to worry about scale-invariant primordial magnetic field models with $\mathrm{B}_{1\ \mathrm{Mpc}} \gtrsim 0.5$ nG when targeting $r \gtrsim 0.001$. The results also show that, as the noise level of the experiment improves, more magnetic field parameter space will be strongly constrained, thus reducing the allowed amplitude of the degenerate primordial magnetic field model.

In Fig. 7 we show how $\Delta\chi^2$ between the two best-fit models changes as we vary r for each of the three sets of

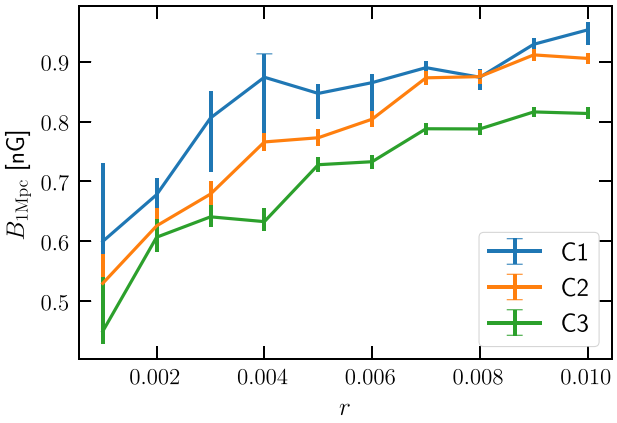

FIG. 6. Magnetic field magnitudes ($\mathrm{B}_{1\ \mathrm{Mpc}}$) that fit the simulated data at different target r for Expt C1, C2, and C3 specified in Table I. The error bars indicate the 68% confidence interval for the marginal posterior distribution.

simulated observations. As a reference, we compare the $\Delta\chi^2$ with the 95% confidence level of a χ^2 distribution with one degree of freedom ($\Delta\chi^2 = -3.841$) since the two competing models differ by one degree of freedom. We note that the estimated $\Delta\chi^2$ for Expt C2 decreases at $r \lesssim 0.004$. This is likely due to a combination of realization-induced randomness and a poor convergence of some of the MCMC chains. Nevertheless, combined with Fig. 6, one sees a generic trend in the decrease of $\mathrm{B}_{1\ \mathrm{Mpc}}$ and the increase of $\Delta\chi^2$ as noise level decreases or as r is lowered, which matches our expectations. Thus, our results are likely sensible approximations of the expected performance of upcoming CMB experiments, which are sufficient for our discussion here. In particular, one can see that the performance of Expt C1 in breaking the degeneracy between the two models quickly degrades as $r \lesssim 0.008$. With C2

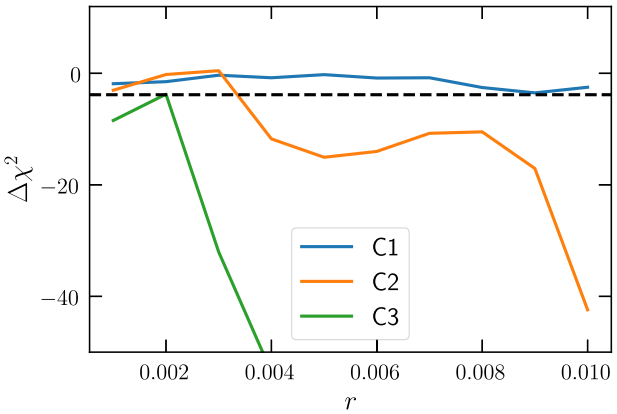

FIG. 7. Variation of $\Delta\chi^2$ with different targets of r. The three lines represent the three simulated sets of observations specified in Table I. The black dashed line shows a reference level of $\Delta\chi^2 = -3.841$ which corresponds to the 95% confidence level for a χ^2 distribution with one degree of freedom.

(a CMB-S4-like experiment), the situation is much improved as the degeneracy is effectively broken for any $r \gtrsim 0.004$. In the noiseless limit (Expt C3), the degeneracy limit in r, after which the two models are indistinguishable, is pushed further down to $r \lesssim 0.002$. This implies that we will be cosmic-variance-limited to make a distinction between an inflationary tensor-mode signal and a primordial magnetic field signal below $r \lesssim 0.002$.

Note that our conclusions so far are based entirely on constraining primordial magnetic fields through their effects on the CMB power spectra by means of metric perturbations and the Lorentz force. However, this is not the only way one can constrain primordial magnetic field signals. In fact, primordial magnetic fields also induce a Faraday rotation effect on the polarization of CMB photons [31], thus providing an additional means to constrain primordial magnetic field models. Hence, in the subsequent sections we will examine whether such an effect can improve our ability to distinguish the two models.

IV. *B*-MODE POLARIZATION FROM FARADAY ROTATION

Another probe of primordial magnetic fields is the effect of Faraday rotation, in which the presence of a magnetic field causes a net rotation of the linear polarization directions of CMB photons along their path. The rotation angle α depends on the frequency of observation and the integrated electron density along the line of sight,

$$\alpha = \frac{3}{16\pi^2 e}\lambda_0^2 \int \dot{\tau}\, \tilde{\mathbf{B}}(\mathbf{x}) \cdot d\boldsymbol{l}, \tag{13}$$

where λ_0 is the observed wavelength, $\dot{\tau} \equiv n_e \sigma_T a$ is the differential optical depth proportional to the electron number density n_e, and $\tilde{\mathbf{B}} \equiv \mathbf{B}a^2$ is the comoving magnetic field. For a homogeneous magnetic field with a present amplitude of $\sim$1 nG, the net rotation of the polarization angle is about a degree at 30 GHz, with the size of the effect scaling with frequency as $\alpha \propto v^{-2}$ [30]. For a stochastic magnetic field with a power spectrum $P_B(k)$, the rotation field $\alpha(\hat{\mathbf{n}})$ is anisotropic with a two-point correlation function given by [53]

$$\langle \alpha(\hat{n})\alpha(\hat{n}')\rangle = \left(\frac{3\lambda_0^2}{16\pi^2 e}\right)^2 \int \frac{d^3k}{(2\pi)^3} P_B(k) \int d\eta \int d\eta' \times \dot{\tau}(\eta)\dot{\tau}(\eta') e^{-i\mathbf{k}\cdot\hat{n}\eta} e^{i\mathbf{k}\cdot\hat{n}'\eta'} [\hat{n}\cdot\hat{n}' - (\hat{k}\cdot\hat{n})(\hat{k}\cdot\hat{n}')], \tag{14}$$

which can also be written as

$$\langle \alpha(\hat{n})\alpha(\hat{n}')\rangle = \sum_L \frac{2L+1}{4\pi} C_L^{\alpha\alpha} P_L(\hat{n}\cdot\hat{n}'), \tag{15}$$

where $P_L(x)$ are the Legendre polynomials and $C_L^{\alpha\alpha}$ is the rotational power spectrum. The rotational power spectrum follows as

$$C_L^{\alpha\alpha} = \left(\frac{3\lambda_0^2}{16\pi^2 e}\right)^2 \frac{2L(L+1)}{\pi} \int_0^\infty \frac{dk}{k} k^3 P_B(k) T_L^2(k), \tag{16}$$

where we have defined a transfer function $T_L(k)$ as

$$T_L(k) \equiv \int_0^{k\Delta\eta} \frac{dx}{x} \dot{\tau}(\eta_0 - x/k) j_L(x). \tag{17}$$

Here η_0 is the conformal time today, $j_L(x)$ is the spherical Bessel function, and $\Delta\eta \equiv \eta_0 - \eta_*$, with η_* corresponding to the conformal time when the visibility function is at its maximum. Equation (16) provides the general expression for the rotational power spectrum generated by a primordial magnetic field model with a given $P_B(k)$.

The rotation field effectively turns E-mode polarization into B-mode polarization, leading to a B-mode power spectrum C_ℓ^{BB} given by [53]

$$C_\ell^{\mathrm{BB}} = \sum_{\ell_2 L} \frac{(2L+1)(2\ell_2+1)}{2\pi} C_L^{\alpha\alpha} C_{\ell_2}^{\mathrm{EE}} (H^L_{\ell\ell_2})^2 \times (1 + (-1)^{L+\ell+\ell_2}), \tag{18}$$

where $H^L_{\ell\ell_2}$ is defined through the Wigner $3j$ symbol [54] as

$$H^L_{\ell\ell_2} \equiv \begin{pmatrix} \ell & L & \ell_2 \\ 2 & 0 & -2 \end{pmatrix}. \tag{19}$$

Equation (18) gives the expected signal in C_ℓ^{BB} from an anisotropic rotation field $\alpha(\hat{\mathbf{n}})$ with a power spectrum $C_L^{\alpha\alpha}$, giving us an additional means to probe the primordial magnetic field model through the Faraday rotation effect.

A. Faraday rotation from a scale-invariant primordial magnetic field

As discussed in Sec. III A, degenerate magnetic field models are approximately scale invariant. Hence, in this section we focus exclusively on this class of primordial magnetic field models (with $n_B \simeq -2.9$). In addition, we make another simplifying assumption that the magnetic modes with scales smaller than the thickness of the last scattering surface contribute negligibly to the total Faraday rotation, so we only consider magnetic modes for $k \lesssim k_D$ with $k_D \simeq 2\ \mathrm{Mpc}^{-1}$. This assumption is motivated by the fact that the total Faraday rotation is dominated by the large-scale modes, as the rotation generated by magnetic modes with scales smaller than the thickness of the last

scattering surface tends to cancel due to the Faraday depolarization effect [55].

With the assumptions above, the transfer function $T_L(k)$ defined in Eq. (17) can then be approximated as

$$T_L(k) \simeq \frac{j_L(k\eta_0)}{k\eta_0}, \tag{20}$$

where we have used the approximation that $\Delta\eta \approx \eta_0$ and the fact that the differential optical depth $\dot{\tau}$ is sharply peaked relative to the slowly varying magnetic field (as we have ignored the fast-varying modes with scales smaller than the thickness of the last scattering surface) and integrates to $\simeq 1$ near the last scattering surface. The rotation power spectrum $C_L^{\alpha\alpha}$ then becomes

$$\begin{aligned} C_L^{\alpha\alpha} &= \frac{9L(L+1)\lambda_0^4}{4(2\pi)^5 e^2 \eta_0^3} \int_0^{k_D} \mathrm{d}k P_B(k) j_L^2(x) \\ &= \frac{9L(L+1)B_\lambda^2 \nu_0^{-4}}{(4\pi)^3 \Gamma(\frac{n_B+3}{2}) e^2} \left(\frac{\lambda}{\eta_0}\right)^{n_B+3} \int_0^{x_D} dx x^{n_B} j_L^2(x), \end{aligned} \tag{21}$$

where $x_D \equiv k_D \eta_0$, ν_0 is the observing frequency, and $\lambda = 1$ Mpc is the length of the smoothing kernel. This result is consistent with that given in Ref. [31]. Specifically, we follow the same approximation as in Ref. [31] that replaces $j_L^2(x)$ with $1/2x^2$ after the second zero of $j_L(x)$ in Eq. (21) to simplify the numerical integration of the fast-oscillating functions. In Fig. 8 we show the rotation power spectrum of a primordial magnetic field with $\mathrm{B}_{1\ \mathrm{Mpc}} = 1$ nG for different n_B, as calculated from Eq. (21). The results show that as the spectral index approaches $n_B \simeq -3$, the rotation spectrum approaches a scale-invariant limit as expected. The above derivations assume that the CMB polarization is generated instantaneously at the beginning of recombination, which is not true. A full calculation also needs to consider that Faraday rotation occurs along with the generation of CMB polarization. This effect was calculated in Ref. [53] and shown to result in a small difference compared to our order-of-magnitude estimate here.

With the rotational power spectrum $C_\ell^{\alpha\alpha}$, one can estimate the expected C_ℓ^{BB} power spectrum sourced by the rotation field using Eq. (18). In Fig. 9 we show the expected B-mode power spectrum sourced by a nearly scale-invariant primordial magnetic field with $n_B = -2.9$ and $\mathrm{B}_{1\ \mathrm{Mpc}} = 1$ nG, observed at 100 GHz.[3] Figure 9 exhibits two noticeable features: (1) the Faraday rotation signal in C_ℓ^{BB} peaks at small angular scales (at $\ell \sim 1000$), similar to the CMB lensing signal, with a significantly lower amplitude than CMB lensing; (2) unlike the CMB lensing signal, the B-mode signal from the rotation field displays acoustic oscillations similar to those in the CMB E-mode power spectrum. This is expected since, according to Eq. (18), the B-mode signal from the rotation field is effectively a convolution of the E-mode power spectrum C_ℓ^{EE} with the rotation power spectrum $C_\ell^{\alpha\alpha}$ in ℓ space. $C_\ell^{\alpha\alpha}$ is scale invariant, so the variation with ℓ in the resulting C_ℓ^{BB} is determined by that of C_ℓ^{EE}, thus reflecting the acoustic oscillations. This is a unique feature that allows to distinguish the rotation signal from the lensing signal in C_ℓ^{BB}.

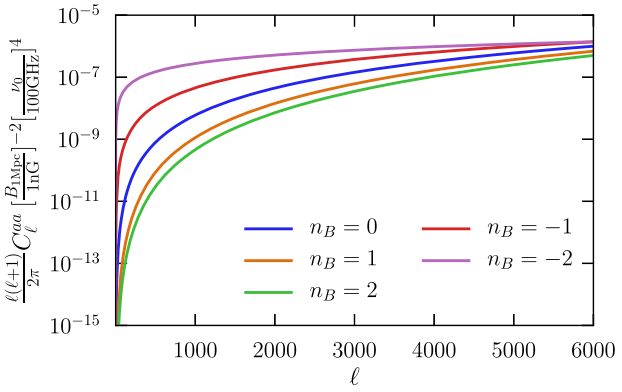

FIG. 8. Rotation power spectrum for different magnetic spectral indices n_B calculated using Eq. (21) with the *Planck* 2018 best-fit cosmology [50], $\nu_0 = 100$ GHz, and $\mathrm{B}_{1\ \mathrm{Mpc}} = 1$ nG. The amplitude of the power spectrum scales with $\mathrm{B}_{1\ \mathrm{Mpc}}^2$ and ν_0^{-4}.

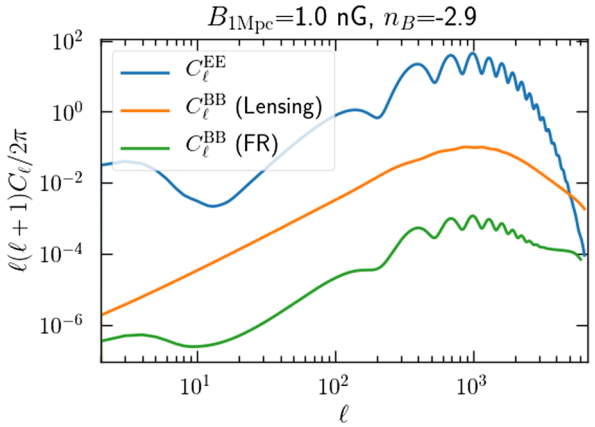

FIG. 9. The green curve shows the B-mode signal (in units of $\mu\mathrm{K}^2$) generated by the Faraday rotation of a primordial magnetic field with $n_B = -2.9$ and $\mathrm{B}_{1\ \mathrm{Mpc}} = 1$ nG at $\nu_0 = 100$ GHz. The orange curve shows the expected lensing signal, and the blue curve shows the C_ℓ^{EE} signal. Note that "FR" denotes Faraday rotation.

[3]Note that we only use the primary E-mode polarization signal to generate the B-mode signal from Faraday rotation. For the small magnetic fields relevant to this paper, the magnetic field contribution to E-mode polarization is negligible compared to the primary CMB E-mode. Therefore, the correction to the Faraday rotation signal from including the magnetic-field E-mode contribution is also negligibly small.

To forecast the expected constraining power of future CMB experiments through Faraday rotation, we define the signal-to-noise ratio (SNR) as

$$\left(\frac{S}{N}\right)^2 = \sum_\ell \frac{(2\ell+1) f_{\rm sky} (C_\ell^{\rm BB,FR})^2}{2(C_\ell^{\rm BB,tot} + N_\ell^{\rm BB})^2}, \tag{22}$$

where $C_\ell^{\rm BB,FR}$ is the expected B-mode signal from Faraday rotation, and $C_\ell^{\rm BB,tot}$ is the total B-mode signal that includes contributions from both the Faraday rotation signal and the CMB lensing signal. $N_\ell^{\rm BB}$ refers to the expected B-mode noise power spectrum from a given experiment as approximated by Eq. (8). The factor $f_{\rm sky}$ is added to approximate the effect of the partial sky coverage of a realistic experiment, in the form of a reduction in the number of available measurements and thus a reduction in the total SNR. In addition, we assume an observing frequency of 100 GHz for the subsequent discussion. Lower frequencies increase the rotation signal for a given magnetic field, but are also technically more difficult to attain comparable map sensitivity and resolution as higher frequency channels like 100 GHz.

As the Faraday rotation signal is mainly significant on small angular scales, large-aperture experiments are most relevant to detecting such a signal. Specifically, we consider Expt B as specified in Table I with different noise levels (6, 2, and 0 μK arcmin), and compute the SNR for each experiment for a scale-invariant primordial magnetic field with the amplitude $B_{1\ \rm Mpc}$ varying from 0.1 to 1 nG. The resulting SNRs are presented in Fig. 10, which shows that for an SO LAT–like experiment with a noise level of 6 μK arcmin, the Faraday rotation signal is not detectable in the power spectrum. In comparison, a CMB-S4-like experiment with a noise level of 2 μK arcmin barely detects a primordial magnetic field with $B_{1\ \rm Mpc} \gtrsim 0.9$ nG at SNR $\gtrsim$1, while in the noiseless limit one can detect a primordial magnetic field with $B_{1\ \rm Mpc} \gtrsim 0.5$ nG with SNR $\gtrsim$1, and $B_{1\ \rm Mpc} \gtrsim 0.8$ nG with SNR $\gtrsim$3. As concluded from Fig. 6, degenerate primordial magnetic field models of interest to the upcoming experiments generally have amplitudes $B_{1\ \rm Mpc}$ ranging from ~0.5–1 nG, comparable to the detection limit of the noiseless case. This suggests that Faraday rotation in the B-mode power spectrum is unlikely a competitive constraint on the primordial magnetic field.

On the other hand, the above SNR estimates neglect the effect of delensing, which is a procedure to remove the CMB lensing signal from the B-mode power spectrum (see, e.g., Ref. [56]). As the CMB lensing signal is generally much larger than the Faraday rotation signal in $C_\ell^{\rm BB}$, being able to remove a significant portion of the lensing signal significantly reduces the total variance in the B-mode power spectrum, thus improving the SNR. To be more specific, we can denote the $C_\ell^{\rm BB,tot}$ in Eq. (22) as

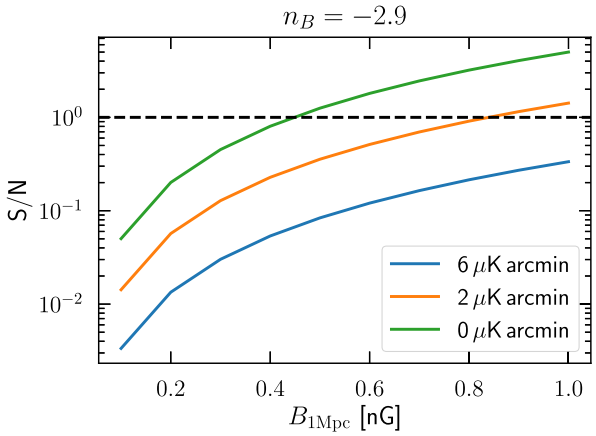

FIG. 10. Signal-to-noise ratio for various $B_{1\ \rm Mpc}$. The three different solid curves show the SNR curve for three experiments with various noise levels. The dashed curve indicates the threshold of SNR = 1.

$$C_l^{\rm BB,tot} = C_l^{\rm BB,CMB} + C_l^{\rm BB,FR} + A_{\rm delens} C_\ell^{\rm BB,lensing}, \tag{23}$$

where $C_l^{\rm BB,CMB}$, $C_\ell^{\rm BB,FR}$, and $C_\ell^{\rm BB,lensing}$ denote the B-mode signal from the CMB, primordial magnetic field, and lensing, respectively, and $A_{\rm delens}$ denotes the residual fraction of delensing which characterizes the delensing efficiency. Optimistic estimates suggest that an SO-like experiment can achieve $A_{\rm delens} \sim 0.5$ with inputs from external data sets [2], and a CMB-S4-like experiment with a noise level around 2 μK arcmin can achieve $A_{\rm delens} \sim 0.4$ [5]. If the B-mode power spectrum is signal dominated, delensing can improve the signal-to-noise ratio by a factor of $A_{\rm delens}^{-1}$, thus lowering the primordial magnetic field detection limit by a factor of $A_{\rm delens}^{-1/2}$.

V. ROTATIONAL FIELD RECONSTRUCTION FROM PRIMORDIAL MAGNETIC FIELDS

Faraday rotation acts as an effective rotation field $\alpha(\hat{\mathbf{n}})$ that rotates the CMB polarization field:

$${}_{\pm2}A(\hat{\mathbf{n}}) \equiv (Q \pm iU)(\hat{\mathbf{n}}) = e^{\pm 2i\alpha(\hat{\mathbf{n}})}(\tilde{Q} \pm i\tilde{U})(\hat{\mathbf{n}}), \tag{24}$$

where Q and U refer to the Stoke parameters for the rotated polarization field and we use a tilde to denote the unrotated polarization field. In the limit that $\alpha(\hat{\mathbf{n}}) \ll 1$, $\delta_{\pm2}A(\hat{\mathbf{n}}) \simeq \pm 2i\alpha(\hat{\mathbf{n}})_{\pm2}\tilde{A}(\hat{\mathbf{n}})$. Such rotation induces off-diagonal correlations between E-mode and B-mode polarization maps [57,58] (see Appendix B for a derivation), given by

$$\langle E_{lm} B^*_{l'm'} \rangle_{\rm CMB} = \sum_{LM} \alpha_{LM} \xi^{LM}_{lml'm'} f^{\rm EB}_{lLl'}, \tag{25}$$

with

$$f^{\mathrm{EB}}_{lLl'} = 2\epsilon_{lLl'}[H^L_{l'l}\tilde{C}^{\mathrm{EE}}_l - H^L_{ll'}\tilde{C}^{\mathrm{BB}}_l], \tag{26}$$

$$\xi^{LM}_{lml_2m_2} \equiv (-1)^m\sqrt{\frac{(2L+1)(2l_2+1)(2l+1)}{4\pi}} \times \begin{pmatrix} l & L & l_2 \\ -m & M & m_2 \end{pmatrix}, \tag{27}$$

and

$$\epsilon_{lLl_2} \equiv \frac{1+(-1)^{l+L+l_2}}{2}. \tag{28}$$

The $\langle\ldots\rangle_{\mathrm{CMB}}$ denotes that the average is to be taken over CMB realizations only. The coupling also allows one to reconstruct the rotation field α_{LM} with a quadratic estimator similar to the reconstruction of CMB lensing [12]:

$$\hat{\alpha}_{LM} = A^{\mathrm{EB}}_L \sum_{ll'}\sum_{mm'} \xi^{LM}_{lml'm'} g^{\mathrm{EB}}_{ll'} E_{lm} B^*_{l'm'}, \tag{29}$$

with the normalization factor A_L defined as

$$(A^{\mathrm{EB}}_L)^{-1} = \sum_{ll'} \frac{(2l+1)(2l'+1)}{4\pi} g^{\mathrm{EB}}_{ll'} f^{\mathrm{EB}}_{lLl'}, \tag{30}$$

ensuring the quadratic estimator is unbiased. The weights $g^{\mathrm{EB}}_{ll'}$ can be chosen to minimize the total variance of the estimator $\langle\alpha^*_{LM}\alpha_{LM}\rangle$ with

$$g^{\mathrm{EB}}_{ll'} = \frac{f^{\mathrm{EB}}_{lLl'}}{C^{\mathrm{EE}}_l C^{\mathrm{BB}}_{l'}}. \tag{31}$$

The minimized variance of the estimator, denoted as N^{EB}_L, is related to the normalization factor as

$$N^{\mathrm{EB}}_L = A^{\mathrm{EB}}_L = \sum_{ll'} \frac{(2l+1)(2l'+1)}{4\pi} \frac{(f^{\mathrm{EB}}_{lLl'})^2}{C^{\mathrm{EE}}_l C^{\mathrm{BB}}_{l'}}, \tag{32}$$

where C^{EE}_l and $C^{\mathrm{BB}}_{l'}$ are the observed E- and B-mode power spectrum, respectively. Here N^{EB}_L is a dimensionless quantity that characterizes the variance of the reconstructed rotation angle at each L.

In Fig. 11, we show the expected reconstruction noise N^{EB}_L calculated using Eq. (32) for experiments considered previously in Table I, and for a nearly scale-invariant primordial magnetic field with varying amplitudes of $\mathrm{B}_{1\ \mathrm{Mpc}}$ and $n_B = -2.9$. In particular, we consider Expt A with noise levels of 2 and 1 μK arcmin, and Expt B with noise levels of 6, 2, and 0 μK arcmin. The results show that the large-aperture experiments have orders of magnitude lower reconstruction noise at $\ell \gtrsim 1000$, confirming our expectation that the small-scale CMB anisotropies dominates the SNR in detecting Faraday rotation signal.

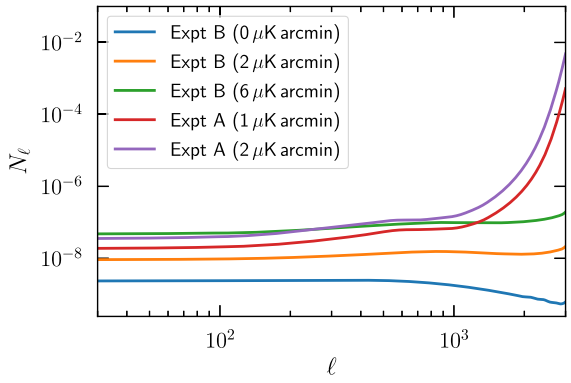

FIG. 11. Gaussian noise covariance N^{EB}_L for experiments specified in Table I with varying noise levels.

To forecast the expected performance of the quadratic estimator for future CMB experiments, we define the SNR as

$$(\mathrm{S/N})^2 = \sum_{L=L_{\mathrm{min}}}^{L_{\mathrm{max}}} f_{\mathrm{sky}} \frac{2L+1}{2}\left(\frac{C^{\alpha\alpha}_L}{N^{EB}_L}\right)^2, \tag{33}$$

where, similar to Sec. IV, we use f_{sky} to approximate the partial sky coverage. We also assume that the observations are made at 100 GHz, which is the frequency channel expected to contribute the highest SNR.

In Fig. 12 we show the expected SNR for the same set of experiments considered previously. It shows that reconstructing a rotation field using the quadratic estimator approach results in an order-of-magnitude improvement in the SNR as compared to constraining its effects on the CMB B-mode power spectrum. This is consistent with the claims in Ref. [59] and is unsurprising as the effect of a rotation field α on C^{BB}_ℓ scales as α^2, which is a second-order effect, whereas its effect on the cross correlation $\langle EB\rangle$ scales with α [see Eq. (25)], which is a first-order effect,

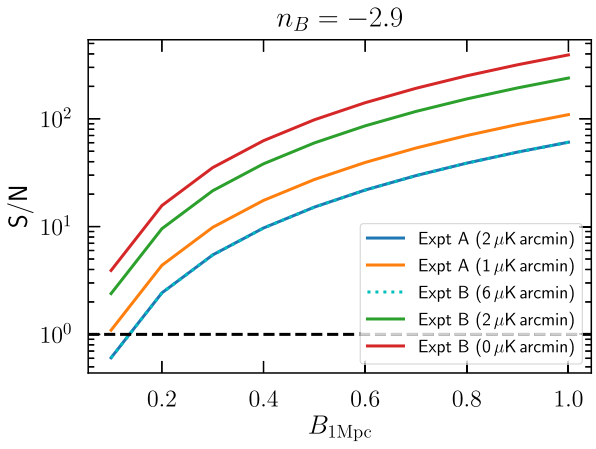

FIG. 12. Signal-to-noise ratio expected for the quadratic estimator in a variety of experimental settings. The black dashed line represents SNR = 1.

thus giving a significantly improved SNR. The results also show that large-aperture experiments (Expt B) have better SNR in general as a result of the significantly lower reconstruction noise (as shown in Fig. 11). Specifically, an SO SAT–like experiment with a noise level of 2 μK arcmin gives comparable SNR to an SO LAT–like experiment with a noise level of 6 μK arcmin, both of which are capable of constraining primordial magnetic field models down to $B_{1\ \mathrm{Mpc}} \gtrsim 0.3$ nG with $S/N \gtrsim 3$. CMB-S4-like noise levels push this limit down to $B_{1\ \mathrm{Mpc}} \gtrsim 0.1$ nG.

These calculations demonstrate that primordial magnetic field models with B-mode power spectra that are degenerate with primordial tensor modes with $r > 0.001$ will be strongly constrained by the rotation signal in small-scale anisotropies. As in Sec. IV, we have neglected the effect of delensing, which may further improve the primordial magnetic field constraint.

VI. DISCUSSION

We have investigated the following question: can primordial magnetic fields be distinguished from primordial gravitational waves as a source of B-mode polarization in the CMB power spectrum? Concerns regarding a possible degeneracy in the B-mode power spectrum signal have previously been raised (see, e.g., Refs. [21,22]). In this work we confirmed with simulations that the answer is likely "no" if one utilizes only the information in the large-scale CMB anisotropies ($\ell \lesssim 1000$), as a primordial magnetic field also introduces large-scale B-mode signals by sourcing tensor-mode metric perturbations in a mathematically equivalent form to that of the primordial gravitational waves, thus generating a completely degenerate signal on large angular scales. However, as we demonstrated in Sec. III, after including small-scale CMB polarization anisotropies ($\ell \gtrsim 1000$), the answer becomes "yes" because of both the magnetic field's vector-mode contribution to B-mode polarization on small scales, and especially due to Faraday rotation of E-mode polarization into B-mode. Upcoming high-sensitivity measurements of polarization on small scales will enable this distinction for any magnetic field that might be mistaken for a primordial tensor mode signal when using only large-angle B-mode polarization data. We demonstrated this explicitly for tensor-mode amplitudes down to $r = 10^{-3}$. For even smaller tensor-mode signals, at some point sufficient delensing techniques must be demonstrated. The amplitude at which lensing signals become an important consideration remains to be seen [60].

As a specific example, we have shown that the power spectrum of a CMB map that covers 40% of the sky with zero noise (cosmic variance limit) can distinguish the presence of a primordial magnetic field equivalent to a tensor mode with amplitude $r \gtrsim 2 \times 10^{-3}$; the same magnetic field can also be detected through its quadratic Faraday rotation signal at a far higher statistical significance, for the same polarization map. The Faraday rotation signal is therefore able to detect the presence of substantially smaller magnetic fields than the power spectrum alone. This is also true in the presence of map noise levels corresponding to near-future experiments. As an example, a BB-polarization power spectrum signal corresponding to a tensor amplitude of roughly $r = 3 \times 10^{-3}$ can be mimicked by a 0.7 nG magnetic field (as shown in Fig. 6). A next-generation CMB experiment, such as Simons Observatory, will have sensitivity for, at best, a marginal detection ($\approx 3.7\sigma$) of this power spectrum signal; such a magnetic field will also produce a Faraday rotation signal which can be detected by quadratic estimation on the same polarization maps with a significance well above 10σ, as shown in Fig. 11.

Our analysis extends previous work (e.g., Ref. [22]) by considering a wider class of magnetic field models and tensor-to-scalar ratio targets and, more importantly, by explicitly identifying degenerate magnetic field models to a given tensor-mode signal using simulations and MCMC-based model fitting. We also for the first time considered map-based Faraday rotation estimation as a way to break the degeneracy between tensor modes and magnetic fields. Our result provides a practical recipe to follow: should a potential tensor-mode signal be detected in the CMB B-mode power spectrum, one can identify degenerate magnetic field models from our analysis and look for its Faraday rotation signal. Upper limits on such a signal provide a clear route to ruling out a plausible contaminant of a tensor B-mode signal. Magnetic fields thus join gravitational lensing and galactic foregrounds as known B-mode contributors for which we possess clear methods of discriminating them from the hallmark signature of early Universe inflation.

ACKNOWLEDGMENTS

We thank Daniel Boyanovsky for helpful comments on the manuscript. Y. G. acknowledges the partial support of Pittsburgh Particle Physics Astrophysics and Cosmology Center (PITT PACC) in the duration of this work. This research was supported in part by the University of Pittsburgh Center for Research Computing through the resources provided.

APPENDIX A: MCMC

We perform MCMC-based model fitting using an ensemble sampler from EMCEE [61] with 50 walkers. We use a mixed proposal function that makes stretch moves 95% of the time and Gaussian moves based on the fisher matrix 5% of the time. We find that the resulting MCMC chains generally converge well after 400 steps based on autocorrelation tests and adopt a fixed number of 400 steps

for all subsequent MCMC runs. Specifically, for the $\Lambda\mathrm{CDM}+r$ model, we adopt flat priors on ω_b, ω_{CDM}, H_0, n_s, A_s, and r, and a Gaussian prior on τ_{reio} with $\tau_{\mathrm{reio}}=0.065\pm0.015$. For the $\Lambda\mathrm{CDM}+\mathrm{PMF}$ model, we use a flat prior on $\mathrm{B}_{1\ \mathrm{Mpc}}$ with $0\leq \mathrm{B}_{1\ \mathrm{Mpc}}\leq 2.5$ nG, and a flat prior on n_B restricted to $-2.9\leq n_B\leq 0$.

In Figs. 13 and 14 we show the full set of posterior distributions for the $\Lambda\mathrm{CDM}+r$ and $\Lambda\mathrm{CDM}+\mathrm{PMF}$ models, respectively, when fitting the simulated observations from Expt A with a fiducial cosmology with a nonzero tensor-to-scalar ratio, $r=0.01$. A burn-in ratio of 70% has been applied to obtain the posterior distributions.

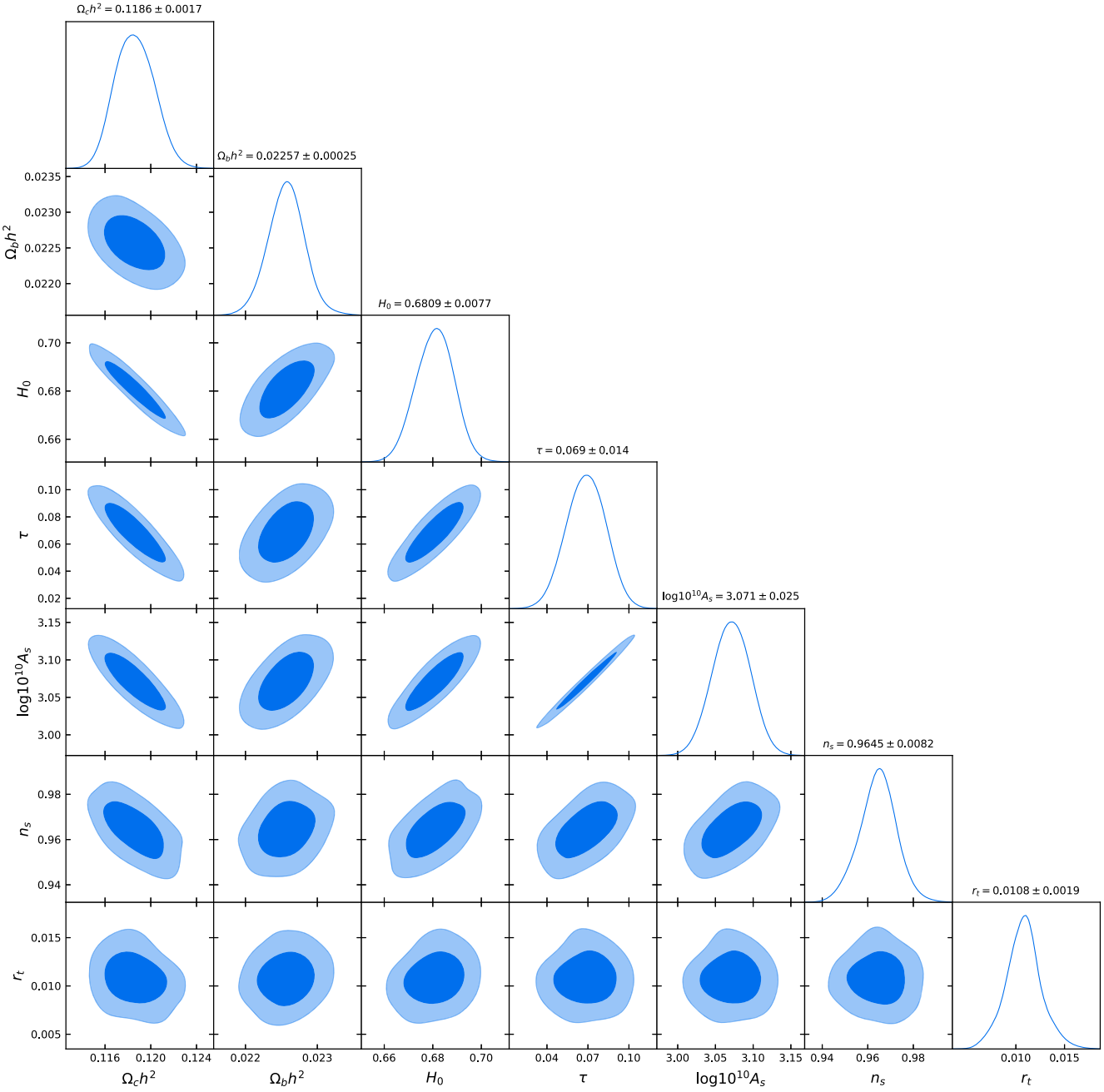

FIG. 13. Best-fit $\Lambda\mathrm{CDM}+r$ cosmological parameters obtained for simulated data for Expt A with a fiducial cosmology with $r=0.010$.

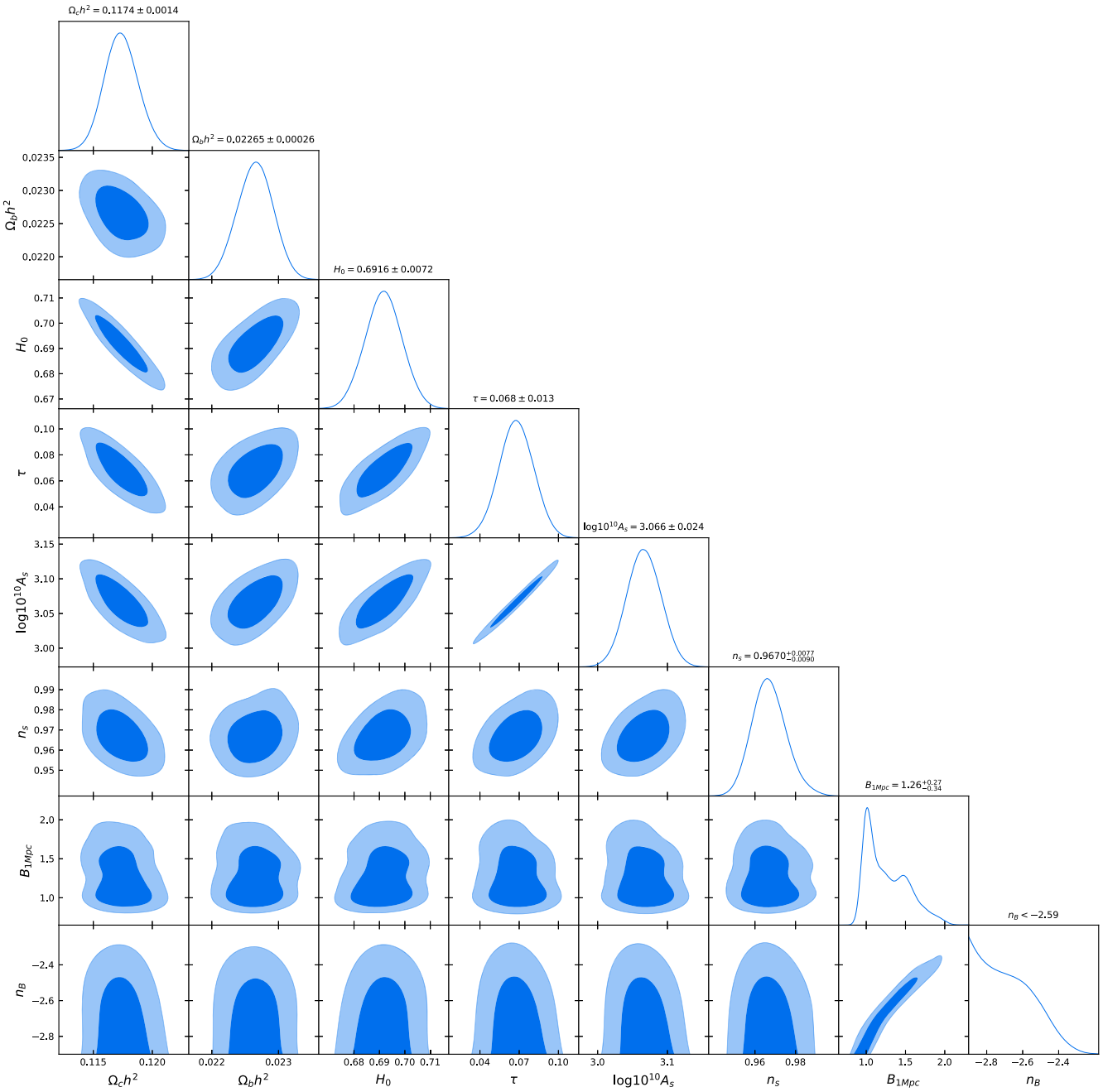

FIG. 14. Best-fit ΛCDM + PMF cosmological parameters obtained for simulated data for Expt A with a fiducial cosmology with $r = 0.010$.

APPENDIX B: QUADRATIC ESTIMATOR FOR POLARIZATION ROTATION

Faraday rotation acts as an effective rotation field $\alpha(\hat{\mathbf{n}})$ that rotates the CMB polarization maps, given by

$$ {}_{\pm 2}A(\hat{\mathbf{n}}) \equiv (Q \pm iU)(\hat{\mathbf{n}}) = e^{\pm 2i\alpha(\hat{\mathbf{n}})}(\tilde{Q} \pm i\tilde{U})(\hat{\mathbf{n}}), \quad \text{(B1)} $$

where Q and U refer to the Stoke parameters for the rotated CMB photons. Approximating α as a small angle, the change in the polarization field due to rotation can be approximated as $\delta({}_{\pm 2}A(\hat{\mathbf{n}})) \simeq \pm 2i\alpha(\hat{\mathbf{n}})\,{}_{\pm 2}\tilde{A}(\hat{\mathbf{n}})$. In lm space, the change in ${}_{\pm 2}A_{lm}$ is

$$ \delta({}_{\pm 2}A_{lm}) \simeq \pm 2i \sum_{\mathrm{LM}} \sum_{l_2 m_2} \alpha_{LM}\, {}_{\pm 2}A_{l_2 m_2} \times \int d\hat{\mathbf{n}}\, {}_{\pm 2}Y^*_{lm}(\hat{\mathbf{n}}) Y_{LM}(\hat{\mathbf{n}})\, {}_{\pm 2}Y_{l_2 m_2}(\hat{\mathbf{n}}), \quad \text{(B2)} $$

where ${}_sY_{lm}$ denotes the spin-weighted spherical harmonics [62]. The integral can be performed with the formula

$$\int d\hat{\mathbf{n}}\, {}_{s_1}Y_{l_1m_1}(\hat{\mathbf{n}})\, {}_{s_2}Y_{l_2m_2}(\hat{\mathbf{n}})\, {}_{s_3}Y_{l_3m_3}(\hat{\mathbf{n}}) = \left[\frac{\prod_{i=1}^{3}2l_i+1}{4\pi}\right]^{1/2}\begin{pmatrix} j_1 & j_2 & j_3 \\ m_1 & m_2 & m_3\end{pmatrix}\begin{pmatrix} j_1 & j_2 & j_3 \\ -s_1 & -s_2 & -s_3\end{pmatrix}, \tag{B3}$$

which gives

$$\delta({}_{\pm2}A_{lm}) \simeq \pm 2i\sum_{LM}\sum_{l_2m_2}\alpha_{LM\,\pm2}A_{l_2m_2}\xi^{LM}_{lml_2m_2\pm}H^L_{ll_2}, \tag{B4}$$

with

$$\xi^{LM}_{lml_2m_2} \equiv (-1)^m\sqrt{\frac{(2L+1)(2l_2+1)(2l+1)}{4\pi}}\begin{pmatrix} l & L & l_2 \\ -m & M & m_2\end{pmatrix}, \tag{B5}$$

and

$${}_{\pm}H^L_{ll_2} \equiv \begin{pmatrix} l & L & l_2 \\ \pm2 & 0 & \mp 2\end{pmatrix} = (-1)^{l+L+l_2}{}_{\mp}H^L_{ll_2}. \tag{B6}$$

On the other hand, the polarization field ${}_{\pm2}A_{lm}$ can be decomposed into curl-free (E-mode) and gradient-free (B-mode) components with

$$\begin{aligned} E_{lm} &= \frac{1}{2}({}_{+2}A_{lm} + {}_{-2}A_{lm}), \\ B_{lm} &= \frac{1}{2i}({}_{+2}A_{lm} - {}_{-2}A_{lm}). \end{aligned} \tag{B7}$$

This gives

$$\delta E_{lm} = -2i\sum_{LM}\sum_{l_2m_2}\alpha_{LM}\xi^{LM}_{lml_2m_2}H^L_{ll_2}(\beta_{lLl_2}\tilde{E}_{l_2m_2} + \epsilon_{lLl_2}\tilde{B}_{l_2m_2}), \tag{B8}$$

and

$$\delta B_{lm} = 2\sum_{LM}\sum_{l_2m_2}\alpha_{LM}\xi^{LM}_{lml_2m_2}H^L_{ll_2}(\epsilon_{lLl_2}\tilde{E}_{l_2m_2} - \beta_{lLl_2}\tilde{B}_{l_2m_2}), \tag{B9}$$

where we have defined $H^L_{ll_2} \equiv {}_{+}H^L_{ll_2}$ and

$$\begin{aligned} \epsilon_{lLl_2} &\equiv \frac{1+(-1)^{l+L+l_2}}{2}, \\ \beta_{lLl_2} &\equiv \frac{1-(-1)^{l+L+l_2}}{2}. \end{aligned} \tag{B10}$$

Equations (B8) and (B9) describe the effect of Faraday rotation on the CMB E-mode and B-mode polarization maps, respectively, which effectively mixes the multipole moments of the two maps through rotation. This introduces couplings between the E-mode and B-mode maps at different l which otherwise do not exist, given by

$$\langle E_{lm}B^*_{l'm'}\rangle_{\rm CMB} = \sum_{LM}\alpha_{LM}\xi^{LM}_{lml'm'}f^{\rm EB}_{lLl'}, \tag{B11}$$

with

$$f^{\rm EB}_{lLl'} = 2\epsilon_{lLl'}[H^L_{l'l}\tilde{C}^{\rm EE}_l - H^L_{ll'}\tilde{C}^{\rm BB}_l]. \tag{B12}$$

The $\langle\ldots\rangle_{\rm CMB}$ denotes that the average is to be taken over CMB realizations only. One can then define an unbiased quadratic estimator for the rotation field as

$$\hat{\alpha}_{LM} = A^{\rm EB}_L\sum_{ll'}\sum_{mm'}\xi^{LM}_{lml'm'}g^{\rm EB}_{ll'}E_{lm}B^*_{l'm'}, \tag{B13}$$

where the normalization factor, which ensures that the estimator is unbiased, is given by

$$(A^{\rm EB}_L)^{-1} = \sum_{ll'}\frac{(2l+1)(2l'+1)}{4\pi}g^{\rm EB}_{ll'}f^{\rm EB}_{lLl'}. \tag{B14}$$

where we have used

$$\sum_{mm'}\xi^{LM}_{lml'm'}\xi^{L'M'}_{lml'm'} = \frac{(2l+1)(2l'+1)}{4\pi}\delta_{LL'}\delta_{MM'}. \tag{B15}$$

[1] F. K. Hansen *et al.*, Planck 2018 results. X. Constraints on inflation, Astron. Astrophys. **641**, A10 (2020).

[2] Peter Ade, James Aguirre, Zeeshan Ahmed, Simone Aiola, Aamir Ali *et al.*, The simons observatory: Science goals and forecasts, J. Cosmol. Astropart. Phys. 02 (2019) 056.

[3] J. A. Grayson, P. A. R. Ade, Z. Ahmed, K. D. Alexander, M. Amiri *et al.*, BICEP3 performance overview and planned Keck Array upgrade, 10.1117/12.2233894 (2016).

[4] M. Hazumi, P. A. R. Ade, Y. Akiba, D. Alonso, K. Arnold *et al.*, LiteBIRD: A satellite for the studies of B-mode polarization and inflation from cosmic background radiation detection, J. Low Temp. Phys. **194**, 443 (2019).

[5] Kevork N. Abazajian, Peter Adshead, Zeeshan Ahmed, Steven W. Allen, David Alonso *et al.*, CMB-S4 Science Book, First Edition (2016), arXiv:1610.02743.

[6] P. A. R. Ade, Z. Ahmed, R. W. Aikin, K. D. Alexander, D. Barkats *et al.*, BICEP2/Keck array V: Measurements of B-mode polarization at degree angular scales and 150 GHz by the Keck Array., Astrophys. J. **811**, 126 (2015).

[7] R. Adam, P. A. R. Ade, N. Aghanim, M. Arnaud, J. Aumont, C. Baccigalupi, A. J. Banday, R. B. Barreiro, J. G. Bartlett *et al.* (Planck Collaboration), Planck intermediate results. XXX. The angular power spectrum of polarized dust emission at intermediate and high Galactic latitudes, Astron. Astrophys. **586**, A133 (2016).

[8] P. A. R. Ade, Z. Ahmed, R. W. Aikin, K. D. Alexander *et al.*, Constraints on Primordial Gravitational Waves Using *Planck*, WMAP, and New BICEP2/Keck Observations Through the 2015 Season, Phys. Rev. Lett. **121**, 221301 (2018).

[9] Lloyd Knox and Yong-Seon Song, Limit on the Detectability of the Energy Scale of Inflation, Phys. Rev. Lett. **89**, 011303 (2002).

[10] D. Hanson, S. Hoover, A. Crites, P. A. R. Ade, K. A. Aird *et al.*, Detection of B-Mode Polarization in the Cosmic Microwave Background with Data from the South Pole Telescope, Phys. Rev. Lett. **111**, 141301 (2013).

[11] Alexander van Engelen, Blake D. Sherwin, Neelima Sehgal, Graeme E. Addison, Rupert Allison *et al.*, The atacama cosmology telescope: Lensing of CMB temperature and polarization derived from cosmic infrared background cross-correlation, Astrophys. J. **808**, 7 (2015).

[12] Wayne Hu and Takemi Okamoto, Mass reconstruction with cosmic microwave background polarization, Astrophys. J. **574**, 566 (2002).

[13] Omar Darwish, Mathew S Madhavacheril, Blake Sherwin *et al.*, The Atacama Cosmology Telescope: A CMB lensing mass map over 2100 square degrees of sky and its cross-correlation with BOSS-CMASS galaxies, 2020, 10.1093/mnras/staa3438.

[14] G. P. Holder *et al.* (SPT Collaboration), A cosmic microwave background lensing mass map and its correlation with the cosmic infrared background, Astrophys. J. **771**, L16 (2013).

[15] N. Aghanim, Y. Akrami, M. Ashdown, J. Aumont *et al.* (Planck Collaboration), Planck 2018 results. VIII. Gravitational lensing, Astron. Astrophys. **641**, A8 (2020).

[16] Gabrielle Simard, Duncan Hanson, and Gil Holder, Prospects for delensing the cosmic microwave background for studying inflation, Astrophys. J. **807**, 166 (2015).

[17] Uroš Seljak and Christopher M. Hirata, Gravitational lensing as a contaminant of the gravity wave signal in the CMB, Phys. Rev. D **69**, 043005 (2004).

[18] David Alonso, Joanna Dunkley, Ben Thorne, and Sigurd Næss, Simulated forecasts for primordial B -mode searches in ground-based experiments, Phys. Rev. D **95**, 043504 (2017).

[19] Marc Kamionkowski and Ely D. Kovetz, The quest for B modes from inflationary gravitational waves, Annu. Rev. Astron. Astrophys. **54**, 227 (2016).

[20] Iain A. Brown, Concerning the statistics of cosmic magnetism, arXiv:1005.2982.

[21] Levon Pogosian and Alex Zucca, Searching for primordial magnetic fields with CMB B-modes, 2018, 10.1088/1361-6382/aac398.

[22] Fabrizio Renzi, Giovanni Cabass, Eleonora Di Valentino, Alessandro Melchiorri, and Luca Pagano, The impact of primordial magnetic fields on future CMB bounds on inflationary gravitational waves, J. Cosmol. Astropart. Phys. 08 (2018) 038.

[23] Lawrence M. Widrow, Origin of galactic and extragalactic magnetic fields, Rev. Mod. Phys. **74**, 775 (2002).

[24] Ruth Durrer and Andrii Neronov, Cosmological magnetic fields: Their generation, evolution and observation, Astron. Astrophys. Rev. **21**, 62 (2013).

[25] Tina Kahniashvili, Axel Brandenburg, Arthur Kosowsky, Sayan Mandal, and Alberto Roper Pol, Magnetism in the Early Universe, 2018, 10.1017/S1743921319004447.

[26] Andrii Neronov and Ievgen Vovk, Evidence for strong extragalactic magnetic fields from fermi observations of TeV blazars, Science **328**, 73 (2010).

[27] Michael S. Turner and Lawrence M. Widrow, Inflation-produced, large-scale magnetic fields, Phys. Rev. D **37**, 2743 (1988).

[28] T. Vachaspati, Magnetic fields from cosmological phase transitions, Phys. Lett. B **265**, 258 (1991).

[29] J. Richard Shaw and Antony Lewis, Massive neutrinos and magnetic fields in the early universe, Phys. Rev. D **81**, 043517 (2010).

[30] Arthur Kosowsky and Abraham Loeb, Faraday rotation of microwave background polarization by a primordial magnetic field, Astrophys. J. **469**, 1 (1996).

[31] Arthur Kosowsky, Tina Kahniashvili, George Lavrelashvili, and Bharat Ratra, Faraday rotation of the cosmic microwave background polarization by a stochastic magnetic field, Phys. Rev. D **71**, 043006 (2005).

[32] Alex Zucca, Yun Li, and Levon Pogosian, Constraints on primordial magnetic fields from planck data combined with the south pole telescope CMB b-mode polarization measurements, Phys. Rev. D **95**, 063506 (2017).

[33] P. A. R. Ade, N. Aghanim, M. Arnaud, F. Arroja, M. Ashdown *et al.*, Planck 2015 results. XIX. Constraints on primordial magnetic fields, Astron. Astrophys. **594**, A19 (2016).

[34] V. B. Semikoz and D. Sokoloff, Magnetic helicity and cosmological magnetic field, Astron. Astrophys. **433**, L53 (2005).

[35] L. Campanelli and M. Giannotti, Magnetic helicity generation from the cosmic axion field, Phys. Rev. D **72**, 123001 (2005).

[36] Axel Brandenburg, Kari Enqvist, and Poul Olesen, Large-scale magnetic fields from hydromagnetic turbulence in the very early Universe, Phys. Rev. D **54**, 1291 (1996).
[37] Robi Banerjee and Karsten Jedamzik, Are Cluster Magnetic Fields Primordial?, Phys. Rev. Lett. **91**, 251301 (2003).
[38] Tina Kahniashvili, Axel Brandenburg, and Alexander G. Tevzadze, The evolution of primordial magnetic fields since their generation, Phys. Scr. **91**, 104008 (2016).
[39] Andrew Mack, Tina Kahniashvili, and Arthur Kosowsky, Microwave background signatures of a primordial stochastic magnetic field, Phys. Rev. D **65**, 123004 (2002).
[40] Massimo Giovannini, Magnetized initial conditions for CMB anisotropies, Phys. Rev. D **70**, 123507 (2004).
[41] Fabio Finelli, Francesco Paci, and Daniela Paoletti, Impact of stochastic primordial magnetic fields on the scalar contribution to cosmic microwave background anisotropies, Phys. Rev. D **78**, 023510 (2008).
[42] Antony Lewis, CMB anisotropies from primordial inhomogeneous magnetic fields, Phys. Rev. D **70**, 043011 (2004).
[43] Camille Bonvin, Chiara Caprini, and Ruth Durrer, Magnetic fields from inflation: The CMB temperature anisotropies, Phys. Rev. D **88**, 083515 (2013).
[44] Massimo Giovannini and Kerstin E. Kunze, Generalized CMB initial conditions with pre-equality magnetic fields, Phys. Rev. D **77**, 123001 (2008).
[45] Massimo Giovannini and Kerstin E. Kunze, Faraday rotation, stochastic magnetic fields, and CMB maps, Phys. Rev. D **78**, 023010 (2008).
[46] Jenni Adams, Ulf H. Danielsson, Dario Grasso, and Héctor Rubinstein, Distortion of the acoustic peaks in the CMBR due to a primordial magnetic field, Phys. Lett. B **388**, 253 (1996).
[47] Tina Kahniashvili and Bharat Ratra, CMB anisotropies due to cosmological magnetosonic waves, Phys. Rev. D **75**, 023002 (2007).
[48] Kerstin E. Kunze, CMB anisotropies in the presence of a stochastic magnetic field, Phys. Rev. D **83**, 023006 (2011).
[49] Antony Lewis, Anthony Challinor, and Anthony Lasenby, Efficient computation of cosmic microwave background anisotropies in closed friedmann-robertson-walker models, Astrophys. J. **538**, 473 (2000).
[50] N. Aghanim, Y. Akrami, M. Ashdown, J. Aumont *et al.* (Planck Collaboration), Planck 2018 results. VI. Cosmological parameters, 2018, 10.1051/0004-6361/201833910.
[51] Samira Hamimeche and Antony Lewis, Likelihood analysis of CMB temperature and polarization power spectra, Phys. Rev. D **77**, 103013 (2008).
[52] Marc Kamionkowski, Arthur Kosowsky, and Albert Stebbins, Statistics of cosmic microwave background polarization, Phys. Rev. D **55**, 7368 (1997).
[53] Levon Pogosian, Amit P. S. Yadav, Yi-Fung Ng, and Tanmay Vachaspati, Primordial magnetism in the CMB: Exact treatment of faraday rotation and WMAP7 bounds, Phys. Rev. D **84**, 043530 (2011).
[54] E P Wigner, *On the Matrices Which Reduce the Kronecker Products of Representations of S. R. Groups* (Springer, Berlin, Heidelberg, 1993), pp. 608–654, ISBN 978-3-662-02781-3.
[55] D. D. Sokoloff, A. A. Bykov, A. Shukurov, E. M. Berkhuijsen, R. Beck, and A. D. Poezd, Depolarization and Faraday effects in galaxies, Mon. Not. R. Astron. Soc. **299**, 189 (1998).
[56] Kendrick M. Smith, Duncan Hanson, Marilena Loverde, Christopher M. Hirata, and Oliver Zahn, Delensing CMB polarization with external datasets, J. Cosmol. Astropart. Phys. 06 (2012) 014.
[57] Marc Kamionkowski, How to Derotate the Cosmic Microwave Background Polarization, Phys. Rev. Lett. **102**, 111302 (2009).
[58] Amit P. S. Yadav, Rahul Biswas, Meng Su, and Matias Zaldarriaga, Constraining a spatially dependent rotation of the cosmic microwave background polarization, Phys. Rev. D **79**, 123009 (2009).
[59] Sayan Mandal, Neelima Sehgal, and Toshiya Namikawa, Finding evidence for inflation and the origin of galactic magnetic fields with CMB surveys, Phys. Rev. D **105**, 063537 (2022).
[60] Hongbo Cai, Yilun Guan, Toshiya Namikawa, and Arthur Kosowsky, Bias from rotation-induced non-gaussianity on lensing reconstruction (to be published).
[61] Daniel Foreman-Mackey, David W. Hogg, Dustin Lang, and Jonathan Goodman, EMCEE: The MCMC hammer, Publ. Astron. Soc. Pac. **125**, 306 (2013).
[62] J. N. Goldberg, A. J. Macfarlane, E. T. Newman, F. Rohrlich, and E. C. G. Sudarshan, Spin-s spherical harmonics and O, J. Math. Phys. (N.Y.) **8**, 2155 (1967).